Modeling of composite plates with an arbitrary hole location using the variable separation method

Philippe Vidal, L. Gallimard, Olivier Polit

Modeling of composite plates with an arbitrary hole location using the variable separation method

P. Vidal *, L. Gallimard, O. Polit

UPL, Univ Paris Nanterre, LEME – Laboratoire Energétique, Mécanique, Electromagnétisme, 92410 Ville d'Avray, France

1. Introduction

Composite structures are widely used in the weight-sensitive industrial applications due to their excellent mechanical properties, especially their high specific stiffness and strength. For many cases of engineering application, the interlaminar stresses are very important for prediction of delamination which is one of the critical failure types of laminated systems. It is also well known that the presence of interlaminar stress components is particularly important in the regions close to free and loaded edges like bolted joints. Thus, a particular attention have to be paid to evaluate precisely their influence on local stress fields in each layer, particularly at the interface between layers.

The pioneering work on straight free-edge problems can be found in the review articles [1,2]. However, due to the complicated geometry and three-dimensional nature of the stresses, laminated composite plates with curved free-edges received relatively less attention. In the following, the references are limited to the works involving the modeling of laminated plate with a hole. Classically, 3D Finite Element (FE) approaches are used [3–7], but the computational cost can increase dramatically as a refined mesh is needed near the hole. Thus, the coupling with 2D approach far from the hole can be carried out [8], but the two regions have to be connected by dedicated formulations. To overcome that, 2D approaches have been developed and can be classified as follows:

- the Equivalent Single Layer Models (ESL): the Reissner-Mindlin (FSDT, [9,10]) and higher-order models (TSDT, [11]) have been addressed. But, only global quantities can be obtained, and the integration of the equilibrium equations is needed to estimate the transverse shear stresses with accuracy. Indeed, transverse shear and normal stress continuity conditions at the interfaces between layers are violated for all of them.
- the Layer-Wise Models (LW): It aims at overcoming the restriction of the ESL concerning the discontinuity of out-of-plane stresses at the interface between adjacent layers. These models are carried out in [11–13] with a high-order expansion of the displacements (at least three). Unfortunately, the number of unknowns depends on the number of layers.

It should be mentioned alternative approaches to overcome high computational cost. For that, the number of unknowns can be reduced by introducing the continuity conditions at the interface layers (on the transverse shear stresses). The so-called Zig-Zag models can be deduced as in [14]. Note also the use of hybrid stress elements based on a mixed form of Hellinger-Reissner principle in [15]. Both ESL and LW approaches are developed.

In this work, a promising alternative approach in the field of the reduced-order modeling based on the separation of variables [16] is performed to overcome these drawbacks and give the solution for any location of the hole. Note that the present study is focused on geometrical modification while preserving the topology of the geometry. One the one hand, it is based on the spatial coordinates separation proposed in [17] and also in [18], and the suitable order

* Corresponding author.
E-mail address: philippe.vidal@parisnanterre.fr (P. Vidal).

http://dx.doi.org/10.1016/j.compstruc.2017.07.020

expansion given in [19–22] for the free-edge effects. On the other hand, a mapping transformation is used for the parameterization of the geometry to refer to a fixed configuration. It has been already carried out in the framework of the reduced basis in [23]. It has been also addressed in [24] with triangular domains for thermal problems and recently in [25] applied to non-straight lines for axisymmetric structures made of isotropic material. These two latter references are related to the proper generalized decomposition method. The present work aims at extending theses approaches to composite plates with a hole which can be considered as a serious challenging benchmark for the designer of layered structures. Thus, a representative test is addressed to assess the reliability and the effectiveness of the present method. The mapping transformation allows us to avoid complex integrations such as in [26]. Another way to solve this problem could be to use the fictitious domain with a indicator function for the hole as in [27]. Nevertheless, we are particularly interested in the transverse stresses near the hole. The representation of this indicator could influence the accuracy of the results in this zone of interest. Thus, this method is not chosen and we will ensure that the quality of the mesh remains good in this zone.

In our approach, the displacements are written under the form of a sum of products of bidimensional polynomials of (x, y), unidimensional polynomials of z and two unidimensional functions of the position of the hole X_T, Y_T. A piecewise fourth-order Lagrange polynomial of z is chosen. A linear interpolation is used for the functions of X_T and Y_T. As far as the variation with respect to the in-plane coordinates is concerned, a 2D eight-node quadrilateral FE is employed. The deduced non-linear problem implies the resolution of four linear problems alternatively. This process yields to a 2D and three 1D problems. Moreover, the explicit solution with respect to the hole position allows us to build a virtual chart in a straightforward manner avoiding the use of numerous expensive LW computations. This could be used to determine the influence of the hole position on the strength failure as in [28]. It could be also seen as a first step towards geometric optimization for laminates.

We now outline the remainder of this article. First, the mechanical formulation is recalled. The parameterization of the hole position requires a mapping transformation which is described. Then, the iterative algorithm to solve the non-linear problem introduced by the variables separation is detailed. The FE discretization is also described. Numerical evaluations are subsequently presented for one-layer and four-layer plate. The behavior of the method is first presented and illustrated. Then, it is assessed to capture local effects and 3D state of the stress, and in particular the transverse stresses near the curved edge, by comparing with reference model available in literature. Results of a LW model issued from Carrera's Unified Formulation [29] are used. Interesting features near the curved free edge can be emphasized even with involving very localized phenomenon.

2. Reference problem description: the governing equations

Let us consider a composite structure occupying the domain $\mathcal{V} = \Omega \times \Omega_z$ with $\Omega = [-a/2, a/2] \times [-b/2, b/2]$ and $\Omega_z = [-h/2, h/2]$ in a Cartesian coordinate (x, y, z). The plate is defined by an arbitrary region Ω in the (x, y) plane, located at the midplane for $z = 0$, and by a constant thickness h. See Fig. 1.

2.1. Constitutive relation

The plate can be made of NC perfectly bonded orthotropic layers. The constitutive equations for a layer k can be written as

$$\boldsymbol{\sigma}^{(k)}(z) = \mathbf{C}^{(k)}\boldsymbol{\varepsilon}(z) \quad \text{for} \quad z \in [z_k, z_{k+1}] \tag{1}$$

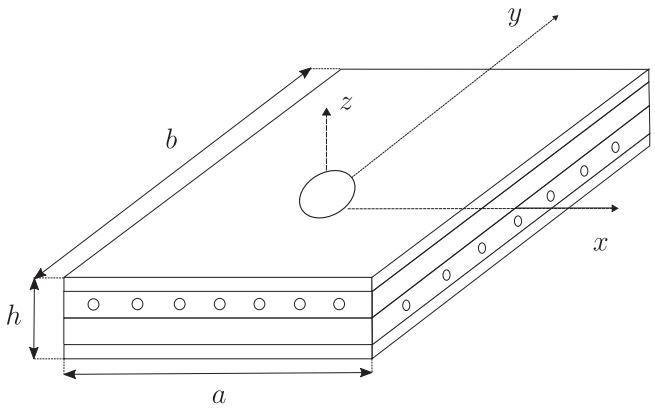

Fig. 1. The laminated plate and coordinate system.

where we denote the stress vector $\boldsymbol{\sigma}$, the strain vector $\boldsymbol{\varepsilon}$. z_k is the z-coordinate of the bottom surface of the layer k.

We have

$$\mathbf{C}^{(k)} = \begin{bmatrix} C_{11}^{(k)} & C_{12}^{(k)} & C_{13}^{(k)} & 0 & 0 & C_{16}^{(k)} \\ & C_{22}^{(k)} & C_{23}^{(k)} & 0 & 0 & C_{26}^{(k)} \\ & & C_{33}^{(k)} & 0 & 0 & C_{36}^{(k)} \\ & & & C_{44}^{(k)} & C_{45}^{(k)} & 0 \\ & sym & & & C_{55}^{(k)} & 0 \\ & & & & & C_{66}^{(k)} \end{bmatrix} \tag{2}$$

where $C_{ij}^{(k)}$ is the three-dimensional stiffness coefficients of the layer (k).

2.2. The weak form of the boundary value problem

The plate is submitted to a surface force density $\mathbf{t}$ defined over a subset Γ_N of the boundary and a body force density $\mathbf{b}$ defined in $\mathcal{V}$. We assume that a prescribed displacement $\mathbf{u} = \mathbf{u}_d$ is imposed on $\Gamma_D = \partial\mathcal{V} - \Gamma_N$.

Using the above matrix notations and for admissible displacement $\delta\mathbf{u} \in \delta U$, the variational principle is given by:

find $\mathbf{u} \in U$ such that:

$$-\int_{\mathcal{V}} \boldsymbol{\varepsilon}(\delta\mathbf{u})^T \boldsymbol{\sigma}\, d\mathcal{V} + \int_{\mathcal{V}} \delta\mathbf{u}^T\mathbf{b}\, d\mathcal{V} + \int_{\Gamma_N} \delta\mathbf{u}^T\mathbf{t}\, d\Gamma = 0 \quad \forall\delta\mathbf{u} \in \delta U \tag{3}$$

where U is the space of admissible displacements, i.e. $U = \{\mathbf{u} \in (H^1(\mathcal{V}))^3 / \mathbf{u} = \mathbf{u}_d \text{ on } \Gamma_D\}$. We have also $\delta U = \{\mathbf{u} \in (H^1(\mathcal{V}))^3 / \mathbf{u} = 0 \text{ on } \Gamma_D\}$.

3. Application of the separated representation to plate with a hole

In this section, we introduce the application of the variables separation for composite plate analysis with an arbitrary hole location. The coordinates of the hole center are considered as parameters of the solution. The main idea consists in using a mapping to refer to a fixed configuration. It has been already used in [25] for parameterized geometry of axisymmetric structures made of isotropic material, and also in [30] for cylindrical shell applications. Moreover, the separated spatial representation [18] is considered with a suitable degree of interpolation of the transverse function for such structures as in [19].

Thus, the classical mechanical problem defined in Section 2 is considered as a parameterized problem where the coordinates of the hole center (X_T, Y_T) is in a bounded interval $\mathcal{I}_T = \mathcal{I}_{TX} \times \mathcal{I}_{TY} = [X_T^m, X_T^M] \times [Y_T^m, Y_T^M]$. The superscripts ^{m} and ^{M} stand for minimum and maximum, respectively. The solution of this problem for a point M of the structure depends on the values of these coordinates and is denoted $\mathbf{u}(x, y, z, X_T, Y_T)$.

3.1. The parameterized problem

The displacement solution $\mathbf{u}$ is constructed as the sum of N products of separated functions ($N \in \mathbb{N}^+$ is the order of the representation)

$$\mathbf{u}(x,y,z,X_T,Y_T) = \sum_{i=1}^{N} g_X^i(X_T) g_Y^i(Y_T)\, \mathbf{f}^i(z) \circ \mathbf{v}^i(x,y) \tag{4}$$

where $g_X^i(X_T), g_Y^i(Y_T), \mathbf{f}^i(z)$ and $\mathbf{v}^i(x,y)$ are unknown functions which must be computed during the resolution process. $g_X^i(X_T), g_Y^i(Y_T), \mathbf{f}^i(z)$ and $\mathbf{v}^i(x,y)$ are defined on $\mathcal{I}_{TX}, \mathcal{I}_{TY}, \Omega_z$ and Ω respectively. As this latter depends on the coordinates (X_T, Y_T), it will be denoted $\Omega(X_T, Y_T)$ (see Fig. 2). The "$\circ$" operator in Eq. (4) is Hadamard's element-wise product. We have:

$$\mathbf{f}^i \circ \mathbf{v}^i = \mathbf{v}^i \circ \mathbf{f}^i = \begin{bmatrix} f_1^i(z)\, v_1^i(x,y) \\ f_2^i(z)\, v_2^i(x,y) \\ f_3^i(z)\, v_3^i(x,y) \end{bmatrix} \quad \text{with} \quad \mathbf{v}^i = \begin{bmatrix} v_1^i(x,y) \\ v_2^i(x,y) \\ v_3^i(x,y) \end{bmatrix}$$
$$\mathbf{f}^i = \begin{bmatrix} f_1^i(z) \\ f_2^i(z) \\ f_3^i(z) \end{bmatrix} \tag{5}$$

For sake of clarity, the body forces are neglected in the developments and the new problem to be solved is written as follows:

find $\mathbf{u} \in \mathcal{U}^{ext}$ $\left(U^{ext} = \{\mathbf{u} \in (H^1(\mathcal{V} \times \mathcal{I}_T))^3 / \mathbf{u} = \mathbf{u}_d \text{ on } \Gamma_D \times \mathcal{I}_T\}\right)$ such that

$$a(\mathbf{u}, \delta\mathbf{u}) = b(\delta\mathbf{u}) \quad \forall \delta\mathbf{u} \in \delta\mathcal{U}^{ext} \tag{6}$$

with

$$a(\mathbf{u}, \delta\mathbf{u}) = \int_{\Omega(X_T,Y_T)\times\Omega_z\times\mathcal{I}_T} \boldsymbol{\varepsilon}(\delta\mathbf{u})^T \mathbf{C} \boldsymbol{\varepsilon}(\mathbf{u})\, d\Omega\, d\Omega_z\, dX_T\, dY_T$$
$$b(\delta\mathbf{u}) = \int_{\Gamma_N\times\mathcal{I}_T} \delta\mathbf{u}^T \mathbf{t}\, d\Gamma\, dX_T\, dY_T \tag{7}$$

where $\Omega(X_T, Y_T) \times \Omega_z \times \mathcal{I}_T$ is the integration space associated with the geometric space domain $\Omega(X_T, Y_T) \times \Omega_z$ and the parameters domain of the hole center coordinates $\mathcal{I}_T$. For the present work, Γ_N is the edge of the plate located at $y = b/2$. At this stage, it should be noted that the integration domain Ω depends on the coordinates of the hole center (X_T, Y_T).

3.2. Introduction of a mapping transformation

As it is highlighted in the previous section, the integration domain in Eq. (7) depends on the parameters X_T, Y_T involved in the unknown function $\mathbf{u}$. To overcome this issue, a mapping transformation is carried out as for optimization problems or shell analysis. So, a transformation $\mathcal{T}_{X_TY_T}(\Omega_0)$ between the domain $\Omega(X_T, Y_T)$ and the reference fixed domain Ω_0 (cf. Fig. 2) is defined. The Jacobian of this transformation appears in the integration, and the strain has to be updated following this choice. The expression of the left hand side of Eq. (6) can be written as

$$\begin{aligned} a(\mathbf{u}, \delta\mathbf{u}) &= \int_{\Omega(X_T,Y_T)\times\Omega_z\times\mathcal{I}_T} \boldsymbol{\varepsilon}(\delta\mathbf{u})^T \mathbf{C} \boldsymbol{\varepsilon}(\mathbf{u})\, d\Omega\, d\Omega_z\, dX_T\, dY_T \\ &= \int_{\Omega_0\times\Omega_z\times\mathcal{I}_T} \boldsymbol{\varepsilon}(\delta\mathbf{u}(\mathcal{T}_{X_TY_T}(\Omega_0)))^T \mathbf{C} \boldsymbol{\varepsilon}(\mathbf{u}(\mathcal{T}(\Omega_0))) \\ &\quad J_{X_TY_T}(\Omega_0)\, d\Omega_0\, d\Omega_z\, dX_T\, dY_T \end{aligned} \tag{8}$$

where $J_{X_TY_T}(\Omega_0)$ is the modulus of the determinant of the geometric transformation Jacobian matrix.

For our application, it should be noted that the geometry will be divided into *NbArea* areas. A domain decomposition Ω_0^p is defined from the initial one Ω_0. In each subdomain, the geometrical transformation remains affine (from Ω_{XY}^p to Ω_0^p, see Fig. 3). Indeed, the integral in Eq. (8) must be split into integrals over each variable, so the expression of $J_{X_TY_T}(\Omega_0)$ must be separated as well. It is an important feature to keep the separability of the variable as it is also noticed in [25]. Moreover, the area around the hole (red part in Fig. 3) is chosen to be fixed to keep the quality of the mesh in this area where out-of-plane stresses occur.

Thus, to express the strain in the reference configuration Ω_0, it is needed to introduce the Jacobian matrix of the geometric transformation. The coordinates associated to the reference frame Ω_0^p and the configuration Ω_{XY}^p will be denoted x, y and X, Y, respectively. This matrix can be written as

$$\mathbf{J}_{\Omega_0^p\Omega_{XY}^p} = \begin{bmatrix} \frac{\partial X}{\partial x} & \frac{\partial X}{\partial y} \\ \frac{\partial Y}{\partial x} & \frac{\partial Y}{\partial y} \end{bmatrix} \tag{9}$$

and the inverse of the Jacobian matrix is introduced:

$$\left[\mathbf{J}_{\Omega_0^p\Omega_{XY}^p}\right]^{-1} = \begin{bmatrix} j_{11}^p & j_{12}^p \\ j_{21}^p & j_{22}^p \end{bmatrix} \tag{10}$$

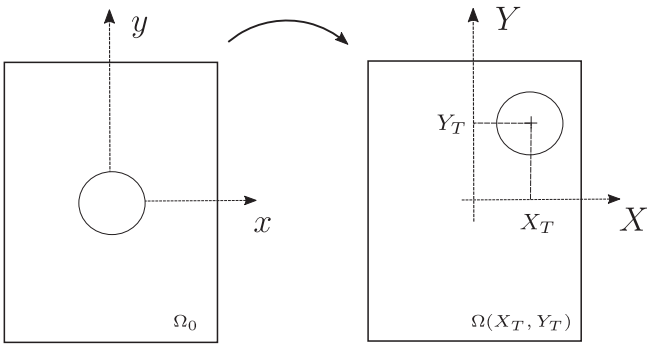

Fig. 2. Mapping transformation.

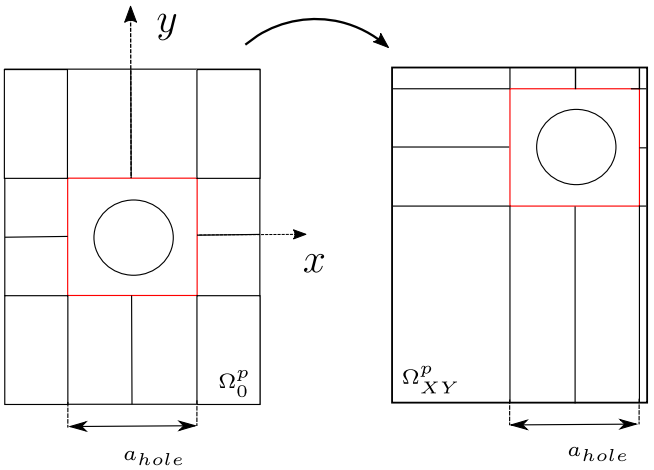

Fig. 3. Division into *NbArea* areas.

Note that the Jacobian matrix is constant. And, it is diagonal in our case due to the particular choice of the sub-domain Ω_0^p (the elements remain rectangular), so $j_{12}^p = j_{21}^p = 0$, for $p \in \{1, \dots, NbArea\}$.

In each sub-domain Ω_0^p, the strain can be expressed with respect to the reference frame with the introduction of the Jacobian of the transformation following

$$\boldsymbol{\varepsilon}(u) = \sum_{i=1}^{N} g_X^i(X_T) g_Y^i(Y_T) \begin{bmatrix} j_{11}^p f_1^i \, v_{1,1}^i \\ j_{22}^p f_2^i \, v_{2,2}^i \\ (f_3^i)' \, v_3^i \\ (f_2^i)' \, v_2^i + j_{22}^p f_3^i \, v_{3,2}^i \\ (f_1^i)' \, v_1^i + j_{11}^p f_3^i \, v_{3,1}^i \\ j_{22}^p f_1^i \, v_{1,2}^i + j_{11}^p f_2^i \, v_{2,1}^i \end{bmatrix} \tag{11}$$

where the prime stands for the classical derivative $\left(f_i' = \frac{df_i}{dz}\right)$, and $()_{,\alpha}$ for the partial derivative. The dependance with respect to the space coordinates is omitted.

3.3. Resolution of the parameterized problem

The expression of the strain Eq. (11) introduced in the problem Eq. (6) drives to a non-linear parameterized problem that is solved by an iterative process. First, we assume that a sum of $m < N$ products of separated functions have been already computed. Therefore, the trial function for the iteration $m+1$ is written as

$$\mathbf{u}^{m+1}(x,y,z,X_T,Y_T) = \mathbf{u}^m(x,y,z,X_T,Y_T) + g_X(X_T) g_Y(Y_T) \mathbf{f}(z) \circ \mathbf{v}(x,y) \tag{12}$$

where $g_X, g_Y, \mathbf{f}$ and $\mathbf{v}$ are the functions to be computed, and $\mathbf{u}^m$ is the associated known sets at iteration m defined by

$$\mathbf{u}^m(x,y,z,X_T,Y_T) = \sum_{i=1}^{n} g_X^i(X_T) g_Y^i(Y_T) \mathbf{f}^{\mathbf{i}}(z) \circ \mathbf{v}^i(x,y) \tag{13}$$

The problem to be solved given in Eq. (7) can be written as

$$a(g_X g_Y \mathbf{f} \circ \mathbf{v}, \delta\mathbf{u}) = b(\delta\mathbf{u}) - a(\mathbf{u}^m, \delta\mathbf{u}) \tag{14}$$

The test function becomes

$$\begin{aligned} \delta(g_X g_Y \mathbf{f} \circ \mathbf{v}) = {} & \delta g_X g_Y \mathbf{f} \circ \mathbf{v} + g_X \delta g_Y \mathbf{f} \circ \mathbf{v} + g_X g_Y \delta\mathbf{f} \circ \mathbf{v} \\ & + g_X g_Y \mathbf{f} \circ \delta\mathbf{v} \end{aligned} \tag{15}$$

Introducing the test function defined by Eq. (15) and the trial function defined by Eq. (12) into the weak form Eq. (14), the four following equations to be solved can be deduced:

- for the test functions δg_X,

$$\begin{aligned} a(g_Y \mathbf{f} \circ \mathbf{v} \, g_X, g_Y \mathbf{f} \circ \mathbf{v} \, \delta g_X) = {} & b(g_Y \mathbf{f} \circ \mathbf{v} \, \delta g_X) \\ & - a(\mathbf{u}^m, g_Y \mathbf{f} \circ \mathbf{v} \, \delta g_X) \quad \forall \delta g_X \end{aligned} \tag{16}$$

- for the test functions δg_Y,

$$\begin{aligned} a(g_X \mathbf{f} \circ \mathbf{v} \, g_Y, g_X \mathbf{f} \circ \mathbf{v} \, \delta g_Y) = {} & b(g_X \mathbf{f} \circ \mathbf{v} \, \delta g_Y) \\ & - a(\mathbf{u}^m, g_X \mathbf{f} \circ \mathbf{v} \, \delta g_Y) \quad \forall \delta g_Y \end{aligned} \tag{17}$$

- for the test function $\delta\mathbf{f}$

$$\begin{aligned} a(g_X g_Y \mathbf{v} \circ \mathbf{f}, g_X g_Y \mathbf{v} \circ \delta\mathbf{f}) = {} & b(g_X g_Y \mathbf{v} \circ \delta\mathbf{f}) \\ & - a(\mathbf{u}^m, g_X g_Y \mathbf{v} \circ \delta\mathbf{f}) \quad \forall \delta\mathbf{f} \end{aligned} \tag{18}$$

- for the test function $\delta\mathbf{v}$

$$\begin{aligned} a(g_X g_Y \mathbf{f} \circ \mathbf{v}, g_X g_Y \mathbf{f} \circ \delta\mathbf{v}) = {} & b(g_X g_Y \mathbf{f} \circ \delta\mathbf{v}) \\ & - a(\mathbf{u}^m, g_X g_Y \mathbf{f} \circ \delta\mathbf{v}) \quad \forall \delta\mathbf{v} \end{aligned} \tag{19}$$

From Eqs. (16)–(19), a coupled non-linear problem is derived. A fixed point method is chosen to solve it. Starting from an initial function $\left(\tilde{g}_X^{(0)}, \tilde{g}_Y^{(0)}, \tilde{\mathbf{f}}^{(0)}, \tilde{\mathbf{v}}^{(0)}\right)$, we construct a sequence $\left(\tilde{g}_X^{(k)}, \tilde{g}_Y^{(k)}, \tilde{\mathbf{f}}^{(k)}, \tilde{\mathbf{v}}^{(k)}\right)$ which satisfy Eqs. (16)–(19) respectively. For each problem, only one unknown 1D or 2D function has to be found, the three other ones are assumed to be known (from the previous step of the fixed point strategy). So, the approach leads to the process given in Algorithm 1. The fixed point algorithm is stopped when the distance between two consecutive terms are sufficiently small (Cf. [19]).

Algorithm 1. Present algorithm

for $m = 1$ to N_{max} **do**
  Initialize $\tilde{g}_Y^{(0)}, \tilde{\mathbf{f}}^{(0)}, \tilde{\mathbf{v}}^{(0)}$
  for $k = 1$ to k_{max} **do**
    Compute $\tilde{g}_X^{(k)}$ from Eq. (16), $\tilde{g}_Y^{(k-1)}, \tilde{\mathbf{f}}^{(k-1)}, \tilde{\mathbf{v}}^{(k-1)}$ being known
    Compute $\tilde{g}_Y^{(k)}$ from Eq. (17), $\tilde{g}_X^{(k)}, \tilde{\mathbf{f}}^{(k-1)}, \tilde{\mathbf{v}}^{(k-1)}$ being known
    Compute $\tilde{\mathbf{f}}^{(k)}$ from Eq. (18) (linear equation on Ω_z), $\tilde{g}_X^{(k)}, \tilde{g}_Y^{(k)}, \tilde{\mathbf{v}}^{(k-1)}$ being known
    Compute $\tilde{\mathbf{v}}^{(k)}$ from Eq. (19) (linear equation on Ω), $\tilde{g}_X^{(k)}, \tilde{g}_Y^{(k)}, \tilde{\mathbf{f}}^{(k)}$ being known
    Check for convergence
  end for
  Set $g_X^{(m+1)} = \tilde{g}_X^{(k)}, g_Y^{(m+1)} = \tilde{g}_Y^{(k)}, \mathbf{f}^{(m+1)} = \tilde{\mathbf{f}}^{(k)}, \mathbf{v}^{(m+1)} = \tilde{\mathbf{v}}^{(k)}$
  Set $\mathbf{u}^{m+1} = \mathbf{u}^m + g_X^{m+1} g_Y^{m+1} \mathbf{f}^{m+1} \circ \mathbf{v}^{m+1}$
  Check for convergence
end for

3.4. Finite element discretization

It should be noted that the initial weakform Eq. (6), Eq. (7) involves multidimensional integrals. As the displacement is assumed to be written under a separated representation (one 2D and three 1D functions), it is needed to separate the calculation of these integrals to achieve an efficient process in terms of computational cost. The three following sections are devoted to show how the expression of the weakform (Eqs. (16)–(19)) can be deduced under this suitable form. Then, the FE discretization can be introduced.

To build the plate finite element approximation, a classical finite element approximation in Ω_0 and Ω_z for $(\mathbf{v}, \mathbf{f})$ is introduced. The elementary vector of degrees of freedom (dof) associated with one element Ω_e of the mesh in Ω_0 is denoted $\mathbf{q}_e^v$. The elementary vector of dofs associated with one element Ω_{z_e} of the mesh in Ω_z is denoted $\mathbf{q}_e^f$. The displacement fields and the strain field are determined from the values of $\mathbf{q}_e^v$ and $\mathbf{q}_e^f$ by

$$\begin{aligned} \mathbf{v}_e &= \mathbf{N}_{xy} \mathbf{q}_e^v, \quad & \boldsymbol{\mathcal{E}}_v^e &= \mathbf{B}_{xy} \mathbf{q}_e^v, \\ \mathbf{f}_e &= \mathbf{N}_z \mathbf{q}_e^f, \quad & \boldsymbol{\mathcal{E}}_f^e &= \mathbf{B}_z \mathbf{q}_e^f \end{aligned} \tag{20}$$

where

$$\boldsymbol{\mathcal{E}}_v^{eT} = [\, v_1 \quad v_{1,1} \quad v_{1,2} \quad v_2 \quad v_{2,1} \quad v_{2,2} \quad v_3 \quad v_{3,1} \quad v_{3,2} \,]$$

$$\boldsymbol{\mathcal{E}}_f^{eT} = [\, f_1 \quad f_1' \quad f_2 \quad f_2' \quad f_3 \quad f_3' \,]$$

The matrices $\mathbf{N}_{xy}, \mathbf{B}_{xy}, \mathbf{N}_z, \mathbf{B}_z$ contain the interpolation functions, their derivatives and the jacobian components.

As far as the functions g_X, g_Y are concerned, a piecewise linear interpolation is considered in $\mathcal{I}_T$

$$g_X(X_T) = \mathbf{N}_{g_X}(X_T)\mathbf{q}^{g_X}, \quad g_Y(Y_T) = \mathbf{N}_{g_Y}(Y_T)\mathbf{q}^{g_Y} \tag{21}$$

where $\mathbf{N}_{g_X}$ and $\mathbf{N}_{g_Y}$ are the matrices of the interpolation functions, $\mathbf{q}^{g_X}, \mathbf{q}^{g_Y}$ are the associated degrees of freedom.

3.5. Finite element problem to be solved on Ω_0

For the sake of simplicity, the functions $\tilde{\mathbf{f}}^{(k)}, \tilde{g}_X^{(k)}, \tilde{g}_Y^{(k)}$ which are assumed to be known, will be denoted $\tilde{\mathbf{f}}, \tilde{g}_X, \tilde{g}_Y$, respectively. And the function $\tilde{\mathbf{v}}^{(k)}$ to be computed will be denoted $\mathbf{v}$. The strains in Eq. (19) are defined as

$$\boldsymbol{\varepsilon}(\tilde{f} \circ v) = \boldsymbol{\Sigma}_{\mathbf{z}}(\tilde{f})\boldsymbol{\mathcal{E}}_v^{\Omega_{XY}} = \boldsymbol{\Sigma}_{\mathbf{z}}(\tilde{f})\mathcal{T}_{\varepsilon}\boldsymbol{\mathcal{E}}_v \tag{22}$$

with

$$\boldsymbol{\Sigma}_{\mathbf{z}}(\tilde{f}) = \begin{bmatrix} 0 & \tilde{f}_1 & 0 & 0 & 0 & 0 & 0 & 0 & 0 \\ 0 & 0 & 0 & 0 & 0 & \tilde{f}_2 & 0 & 0 & 0 \\ 0 & 0 & 0 & 0 & 0 & 0 & \tilde{f}'_3 & 0 & 0 \\ 0 & 0 & 0 & \tilde{f}'_2 & 0 & 0 & 0 & 0 & \tilde{f}_3 \\ \tilde{f}'_1 & 0 & 0 & 0 & 0 & 0 & 0 & \tilde{f}_3 & 0 \\ 0 & 0 & \tilde{f}_1 & 0 & \tilde{f}_2 & 0 & 0 & 0 & 0 \end{bmatrix} \tag{23}$$

$\mathcal{T}_{\varepsilon}$ contains the components of the inverse of the jacobian matrix, namely $j_{ii}^p,\ i = 1, 2$. It can be deduced from Eq. (11). It is not detailed here as it is only used for convenience in the expression of the strain and one integral. In practice, the problem has to be written in a more suitable way as it is described below.

The variational problem defined on Ω_0 from Eq. (19) is

$$\begin{aligned} &\sum_{p=1}^{NbArea} \int_{\Omega_0^p} \left[\delta\boldsymbol{\mathcal{E}}_v^T \mathbf{k}_{zXY}^p(\tilde{f}, \tilde{g}_X, \tilde{g}_Y)\boldsymbol{\mathcal{E}}_v\right] d\Omega_0^p \\ &\quad = \sum_{p=1}^{NbAreaPres} \int_{\Gamma_N^p} t_{X_T Y_T}^p \delta\mathbf{v}^T \mathbf{t}_z(\tilde{f}) dS^p \\ &\quad\quad - \sum_{p=1}^{NbArea} \int_{\Omega_0^p} \left[\delta\boldsymbol{\mathcal{E}}_v^T \boldsymbol{\sigma}_{zXY}^p(\tilde{f}, \tilde{g}_X, \tilde{g}_Y, \mathbf{u}^m)\right] d\Omega_0^p \end{aligned} \tag{24}$$

where

$$\mathbf{k}_{zXY}^p(\tilde{f}, \tilde{g}_X, \tilde{g}_Y) = \sum_{\substack{1\leqslant i\leqslant 3 \\ 1\leqslant j\leqslant 3 \\ i\leqslant j}} \mathbf{k}_z(\tilde{f}) \circ \mathbf{U}_{ij} \int_{X_T} \tilde{g}_X^2 T_{Xij}^p dX_T \int_{Y_T} \tilde{g}_Y^2 T_{Yij}^p dY_T \tag{25}$$

and

$$\begin{aligned} \mathbf{t}_z(\tilde{f}) &= \int_{\Omega_z} \tilde{\mathbf{f}} \circ \mathbf{t}\, dz \\ \boldsymbol{\sigma}_{zXY}^p(\tilde{f}, \tilde{g}_X, \tilde{g}_Y, \mathbf{u}^m) &= \int_{X_T} \int_{Y_T} \int_{\Omega_z} \left[\tilde{g}_X \tilde{g}_Y \mathcal{T}_{\varepsilon}^T \boldsymbol{\Sigma}_{\mathbf{z}}(\tilde{f})^T \mathbf{C}\boldsymbol{\varepsilon}(\mathbf{u}^m)\right] dz\, dX_T\, dY_T \\ t_{X_T Y_T}^p &= \int_{X_T} \tilde{g}_X T_{X11}^p dX_T \int_{Y_T} \tilde{g}_Y\, dY_T \end{aligned} \tag{26}$$

$\mathbf{k}_z(\tilde{f})$ and the 9×9 matrix $\mathbf{U}_{\mathbf{ij}}$ are defined by

$$\begin{aligned} \mathbf{k}_z(\tilde{f}) &= \int_{\Omega_z} \boldsymbol{\Sigma}_{\mathbf{z}}(\tilde{f})^T \mathbf{C} \boldsymbol{\Sigma}_{\mathbf{z}}(\tilde{f}) dz \\ \mathbf{U}_{\mathbf{ij}} &= \begin{bmatrix} \mathbf{H_{ij}} & \mathbf{H_{ij}} & \mathbf{H_{ij}} \\ \mathbf{H_{ij}} & \mathbf{H_{ij}} & \mathbf{H_{ij}} \\ \mathbf{H_{ij}} & \mathbf{H_{ij}} & \mathbf{H_{ij}} \end{bmatrix} \text{ with } (h_{ij})_{kl} \begin{cases} = 1 & \text{if } k = i, l = j \\ & \text{or } k = j, l = i \\ = 0, & \text{otherwise} \end{cases} \end{aligned} \tag{27}$$

The expression of T_{Xij}^p and T_{Yij}^p are given in Appendix A.

It should be noted that the expression of $\mathbf{k}_{zXY}^p(\tilde{f}, \tilde{g}_X, \tilde{g}_Y)$ introduced in Eq. (25) is split into 6 matrices. It allows us to obtain a separated representation which is particularly suitable to the present formulation.

Note that $\boldsymbol{\sigma}_{zXY}^p$ is also expressed under a separated form to keep the computational efficiency of the method. For this purpose, the same principle as the computation of $\mathbf{k}_{zXY}^p$ is performed. It is detailed in Appendix B.

The introduction of the finite element approximation Eq. (20) in the variational Eq. (24) leads to the linear system

$$\mathbf{K}_{zXY}(\tilde{f}, \tilde{g}_X, \tilde{g}_Y)\mathbf{q}^v = \boldsymbol{\mathcal{R}}_t(\tilde{f}, \tilde{g}_X, \tilde{g}_Y) - \boldsymbol{\mathcal{R}}_v(\tilde{f}, \tilde{g}_X, \tilde{g}_Y, \mathbf{u}^m) \tag{28}$$

where

- $\mathbf{q}^v$ is the vector of the nodal displacements, associated with the finite element mesh in Ω_0,
- $\mathbf{K}_{zXY}(\tilde{f}, \tilde{g}_X, \tilde{g}_Y)$ is the mechanical stiffness matrix obtained by summing the elements' stiffness matrices $\mathbf{K}_{zXY}^e(\tilde{f}, \tilde{g}_X, \tilde{g}_Y) = \int_{\Omega_e} \left[\mathbf{B}_{xy}^T \mathbf{k}_{zXY}^p(\tilde{f}, \tilde{g}_X, \tilde{g}_Y)\mathbf{B}_{xy}\right] d\Omega_e$
- $\boldsymbol{\mathcal{R}}_t(\tilde{f}, \tilde{g}_X, \tilde{g}_Y) - \boldsymbol{\mathcal{R}}_v(\tilde{f}, \tilde{g}_X, \tilde{g}_Y, \mathbf{u}^m)$ is the equilibrium mechanical residual obtained by summing the elements' load vectors $\int_{\Gamma_e} \mathbf{N}_{xy}^T \mathbf{t}_z(\tilde{f}) d\Gamma_e$ and $\int_{\Omega_e} \mathbf{B}_{xy}^T \boldsymbol{\sigma}_{zXY}^p(\tilde{f}, \tilde{g}_X, \tilde{g}_Y, \mathbf{u}^m) d\Omega_e$ (associated to the known terms)

3.6. Finite element problem to be solved on Ω_z

As in the previous section, the known functions $\tilde{\mathbf{v}}^{(k-1)}, \tilde{g}_X^{(k)}, \tilde{g}_Y^{(k)}$ will be denoted $\tilde{\mathbf{v}}, \tilde{g}_X, \tilde{g}_Y$, and the functions $\tilde{\mathbf{f}}^{(k)}$ to be computed will be denoted $\mathbf{f}$. The strain in Eq. (18) is defined as

$$\boldsymbol{\varepsilon}(\tilde{v} \circ f) = \boldsymbol{\Sigma}_{\mathbf{xy}}^{\boldsymbol{\Omega}_{\mathbf{XY}}}(\tilde{v})\boldsymbol{\mathcal{E}}_f = \mathcal{T}_{\Sigma}\boldsymbol{\Sigma}_{\mathbf{xy}}^{\boldsymbol{\Omega}_{\mathbf{0}}}(\tilde{v})\boldsymbol{\mathcal{E}}_f \tag{29}$$

where $\mathcal{T}_{\Sigma}$ is the transformation of the derivatives from Ω_0^p to Ω_{XY}^p, and

$$\boldsymbol{\Sigma}_{\mathbf{xy}}^{\boldsymbol{\Omega}_{\mathbf{0}}}(\tilde{v}) = \begin{bmatrix} \tilde{v}_{1,1} & 0 & 0 & 0 & 0 & 0 \\ 0 & 0 & \tilde{v}_{2,2} & 0 & 0 & 0 \\ 0 & 0 & 0 & 0 & 0 & \tilde{v}_3 \\ 0 & 0 & 0 & \tilde{v}_2 & \tilde{v}_{3,2} & 0 \\ 0 & \tilde{v}_1 & 0 & 0 & \tilde{v}_{3,1} & 0 \\ \tilde{v}_{1,2} & 0 & \tilde{v}_{2,1} & 0 & 0 & 0 \end{bmatrix} \tag{30}$$

As in the previous section, $\mathcal{T}_{\Sigma}$ is only introduced by convenience.

The variational problem defined on Ω_z from Eq. (18) is

$$\begin{aligned} \int_{\Omega_z} \delta\boldsymbol{\mathcal{E}}_f^T \mathbf{k}_{xyXY}(\tilde{v}, \tilde{g}_X, \tilde{g}_Y)\boldsymbol{\mathcal{E}}_f\, dz &= \int_{\Omega_z} \delta\mathbf{f}^T \mathbf{t}_{xyXY}(\tilde{v}, \tilde{g}_X, \tilde{g}_Y) dz \\ &\quad - \int_{\Omega_z} \delta\boldsymbol{\mathcal{E}}_f^T \boldsymbol{\sigma}_{xyXY}(\tilde{v}, \tilde{g}_X, \tilde{g}_Y, \mathbf{u}^m) dz \end{aligned} \tag{31}$$

where $\mathbf{k}_{xyXY}(\tilde{v}, \tilde{g}_X, \tilde{g}_Y)$ can be expressed under the following separated form:

$$\mathbf{k}_{xyXY}(\tilde{v}, \tilde{g}_X, \tilde{g}_Y) = \sum_{\substack{1\leqslant i\leqslant 3 \\ 1\leqslant j\leqslant 3 \\ i\leqslant j}} \sum_{p=1}^{NbArea} \mathbf{k}_{xy\,ij}^p(\tilde{v}) \int_{X_T} \tilde{g}_X^2 T_{Xij}^p dX_T \int_{Y_T} \tilde{g}_Y^2 T_{Yij}^p dY_T \tag{32}$$

$\mathbf{k}_{xy\,ij}^p(\tilde{v})$ is obtained by integrating the functions $\tilde{v}_i,\ i\epsilon\{1, 3\}$ over each area defined in Fig. 3 and depends on the three-dimensional stiffness coefficients.

We also define:

$$\mathbf{t}_{xyXY}(\tilde{v},\tilde{g}_X,\tilde{g}_Y) = \sum_{p=1}^{NbArea} t^p_{X_TY_T} \int_{\Gamma_N^p} \tilde{\mathbf{v}} \circ \mathbf{t}\, dx^p$$

$$\boldsymbol{\sigma}_{xyXY}(\tilde{v},\tilde{g}_X,\tilde{g}_Y,\mathbf{u}^m) = \sum_{p=1}^{NbArea} \int_{\Omega_0^p} \int_{\mathcal{I}_T} \left[\tilde{g}_X \tilde{g}_Y\, \boldsymbol{\Sigma}^{\boldsymbol{\Omega_0}}_{\mathbf{xy}}(\tilde{v})^T \mathcal{T}_\Sigma^T(\mathbf{C}\boldsymbol{\varepsilon}(\mathbf{u}^m))\right] dX_T\, dY_T\, d\Omega_0^p \tag{33}$$

The term $\boldsymbol{\sigma}_{xyXY}(\tilde{v},\tilde{g}_X,\tilde{g}_Y,\mathbf{u}^m)$ is given under a short form for convenience reason, but it can also be written under a separated representation following the same decomposition as in Eq. (32).

The introduction of the finite element discretization Eq. (20) in the variational Eq. (31) leads to the linear system

$$\mathbf{K}_{xyXY}(\tilde{v},\tilde{g}_X,\tilde{g}_Y)\mathbf{q}^f = \boldsymbol{\mathcal{R}}_{ft}(\tilde{v},\tilde{g}_X,\tilde{g}_Y) - \boldsymbol{\mathcal{R}}_f(\tilde{v},\tilde{g}_X,\tilde{g}_Y,\mathbf{u}^m) \tag{34}$$

where

- $\mathbf{q}^f$ is the vector of degree of freedom associated with the F.E. approximations in Ω_z.
- $\mathbf{K}_{xyXY}(\tilde{v},\tilde{g}_X,\tilde{g}_Y)$ is obtained by summing the elements' stiffness matrices:

$$\mathbf{K}^e_{xyXY}(\tilde{v},\tilde{g}_X,\tilde{g}_Y) = \int_{\Omega_{ze}} \left[\mathbf{B}_z^T \mathbf{k}_{xyXY}(\tilde{v},\tilde{g}_X,\tilde{g}_Y)\mathbf{B}_z\right] dz_e \tag{35}$$

- $\boldsymbol{\mathcal{R}}_{ft}(\tilde{v},\tilde{g}_X,\tilde{g}_Y) - \boldsymbol{\mathcal{R}}_f(\tilde{v},\tilde{g}_X,\tilde{g}_Y,\mathbf{u}^m)$ is a equilibrium residual, it is obtained by the summation of the elements' residual vectors coming from the right hand side of Eq. (33).

3.7. Finite element problem to be solved on $\mathcal{I}_T$

In this part, we will focus on the computation of the unknown function $\tilde{g}_X^{(k)}$, denoted g_X, the other ones $\tilde{\mathbf{v}}^{(k-1)}, \tilde{\mathbf{f}}^{(k-1)}, \tilde{g}_Y^{(k-1)}$ being known. They are denoted $\tilde{\mathbf{v}}, \tilde{\mathbf{f}}$ and $\tilde{g}_Y$, respectively.

The problem Eq. (16) can be solved in a straightforward manner following:

$$K_{xyzY}(\tilde{v},\tilde{f},\tilde{g}_Y)\, g_X = \mathcal{R}_{g_Xt}(\tilde{v},\tilde{f},\tilde{g}_Y) - \mathcal{R}_{g_X}(\tilde{v},\tilde{f},\tilde{g}_Y,\mathbf{u}^m) \tag{36}$$

where we have

- the stiffness matrix

$$K_{xyzY}(\tilde{v},\tilde{f},\tilde{g}_Y) = \sum_{p=1}^{NbArea} \sum_{\substack{1\leqslant i\leqslant 3\\ 1\leqslant j\leqslant 3\\ i<j}} E^p_{z\Omega ij}(\tilde{f},\tilde{v}) \left[\int_{Y_T} \tilde{g}_Y^2\, T^p_{Yij}\, dY_T\right] T^p_{Xij}\Big|_{X_T} \tag{37}$$

with

$$E^p_{z\Omega ij}(\tilde{f},\tilde{v}) = \int_{\Omega_0^p} \tilde{\mathcal{E}}_{\mathbf{v}}^T \left[\mathbf{k}_z(\tilde{f}) \circ \mathbf{U}_{\mathbf{ij}}\right] \tilde{\mathcal{E}}_{\mathbf{v}}\, d\Omega_0^p \tag{38}$$

$\mathbf{k}_z(\tilde{f})$ and $\mathbf{U}_{\mathbf{ij}}$ are given in Eq. (27).

- the equilibrium residual

$$\mathcal{R}_{g_Xt}(\tilde{v},\tilde{f},\tilde{g}_Y) = \left[\sum_{p=1}^{NbArea} \int_{\Gamma_N^p} \tilde{\mathbf{v}}^T dx^p\, T^p_{X11}|_{X_T}\right] \mathbf{t}_z(\tilde{f}) \int_{Y_T} \tilde{g}_Y\, dY_T \tag{39}$$

$$\mathcal{R}_{g_X}(\tilde{v},\tilde{f},\tilde{g}_Y,\mathbf{u}^m) = \sum_{p=1}^{NbArea} \int_{Y_T} \int_{\Omega_0^p} \int_{\Omega_z} \left[\tilde{g}_Y\, \tilde{\mathcal{E}}_{\mathbf{v}}^T \mathcal{T}_\varepsilon^T \boldsymbol{\Sigma}_{\mathbf{z}}(\tilde{f})^T \mathbf{C}\boldsymbol{\varepsilon}(\mathbf{u}^m)\right] dz\, d\Omega_0^p\, dY_T \tag{40}$$

$\mathcal{R}_{g_X}(\tilde{v},\tilde{f},\tilde{g}_Y,\mathbf{u}^m)$ is built from the known function $\mathbf{u}^m$. It is computed in the same way as K_{xyzY} to deduce a separated representation.

The computation of the unknown function $\tilde{g}_Y^{(k)}$ is given in Appendix C. We can notice that the computational cost of this problem is very low once the problem associated to $\tilde{g}_X^{(k)}$ is solved. In fact, the computational cost comes mainly from the evaluation of the $6 \times NbArea$ scalar values $E^p_{z\Omega ij}(\tilde{f},\tilde{v})$ which have been already computed and stored in the $\tilde{g}_X^{(k)}$ problem.

4. Numerical results

This section is devoted to the assessment of the present approach for static response of composite plates with a hole. The example involved in this work is a challenging test in the modeling of such structures. The separated representation has already shown interesting features in the framework of free-edge effects (see [22]) and also for parametric geometry [25]. Thus, it is interesting to extend the method to a variable geometry for anisotropic structure where high stress gradient occurs.

In the numerical examples, an eight-node quadrilateral FE based on the classical Serendipity interpolation functions is used for the unknowns depending on the in-plane coordinates. For the unknowns depending on the z-coordinate, the displacement is described by a fourth-order interpolation as it is justified in [19]. A Gaussian numerical integration with 3×3 points is used to evaluate the elementary matrices. As far as the integration with respect to the transverse coordinate is concerned, an analytical integration is performed.

The results are compared with a fourth-order LayerWise model (denoted LD4) referring to the systematic work of Carrera and his "Carrera's Unified Formulation" (CUF), (see [31,32]). It can be considered as reference results. Firstly, the behavior of the method is illustrated on a one layer plate. A convergence study is carried out. Then, the capabilities of the approach are assessed on a 4-layer cross-ply structure and in particular, the accuracy of the out-of-plane stresses occurring in the vicinity of the hole is shown.

Note that the use of subdomains with a fixed area around the hole allows us to have a simple translation in the geometrical transformation described in Section 3.2. So, the size of the elements remains unchanged near the zone of interest and no additional error is introduced by the mapping transformation in this region, as the mesh will not be distorted. However, the usual errors hold.

4.1. Description of the test case

A plate with a circular hole subjected to a uniaxial tension in the longitudinal direction is considered. The angle θ is defined from the $x-axis$ (see Fig. 4). The test is described below:

geometry: rectangular composite cross-ply plate $[0^\circ]$ or $[0^\circ/90^\circ/90^\circ/0^\circ]$ the radius of the hole is $R = 3$ m. All layers have the same thickness. $h = 2$ m, $a = 20$ m, $b = 40$ m.
boundary conditions: clamped on one side ($y = -b/2$) and subjected to a constant pressure $q_y(x, b/2) = q_0$
material properties: $E_L = 25$ GPa, $E_T = 1$ GPa, $G_{LT} = 0.2$ GPa, $G_{TT} = 0.5$ GPa, $\nu_{LT} = \nu_{TT} = 0.25$ where L refers to the fiber direction, T refers to the transverse direction.
mesh: the whole plate is meshed. $N_{theta} = 10$ elements on a quarter of the hole. The size of the central part is $a_{hole} = 10$ m (Fig. 3).

number of dofs: mesh 1: one-layer case $Ndof_{xy} = 5616$ and $Ndof_z = 12 \times NC + 3 = 15$mesh 2: our-layer case $Ndof_{xy} = 16,056$ and $Ndof_z = 12 \times NC + 3 = 51$
reference values: LD4 (one-layer case $NdofLD4_{xy} = 28,080$; four-layer case $NdofLD4_{xy} = 272,952$)

If not mentioned, the dimensional quantities are expressed in SI units.

4.2. The one-layer case

The approach is first assessed on a one-layered plate where the coordinates of the hole center belongs to the interval $\mathcal{I}_T = [-4,4] \times [-12,12]$. It allows us to consider a wide range of variation for the position of the hole. A convergence study is performed with respect to the number of elements associated to the functions g_X and g_Y, denoted NDF_{XYT}. For a fixed value of X_T, Y_T, a local error indicator between a reference solution $\mathbf{u}^{ref}$ and a separated variables solution $\mathbf{u}^n$ of order n is introduced as

$$\epsilon_n = 100\sqrt{\frac{a_{err}(\mathbf{u}^n - \mathbf{u}^{ref}, \mathbf{u}^n - \mathbf{u}^{ref})}{a_{err}(\mathbf{u}^{ref}, \mathbf{u}^{ref})}} \quad \text{with } a_{err}(\mathbf{u},\mathbf{v}) = \int_{\Omega\times\Omega_z} \boldsymbol{\varepsilon}(\mathbf{v})^T \mathbf{C} \boldsymbol{\varepsilon}(\mathbf{u}) d\Omega\, d\Omega_z \tag{41}$$

The variation of this error indicator with respect to the number of the iterations is represented on Fig. 5 for $(X_T = -4, Y_T = -12), (X_T = 0, Y_T = 0), (X_T = 4, Y_T = 12)$ and for different values of NDF_{XYT}. It corresponds to the bounds of the interval for the variation of the position of the hole center. The trend of these three configurations is rather similar. Thus, the influence of NDF_{XYT} is not significant for this range. Moreover, we notice that the configuration with the hole at the center of the plate (namely Ω_0) drives to the lowest error rate. In the following, 65 terms are built to obtain the solution.

For further investigations, the contribution of each 4-uplets in the total strain energy $\Delta E(m) = \frac{a_{err}(\mathbf{u}^m,\mathbf{u}^m) - a_{err}(\mathbf{u}^{m-1},\mathbf{u}^{m-1})}{a_{err}(\mathbf{u}^N,\mathbf{u}^N)}$ is shown in Fig. 6 for the three locations of the hole. The main contributions are brought by the first 4-uplets, in particular for $(X_T = 0, Y_T = 0)$ where 99% of the energy is included in the first 5 couples. Nevertheless, depending on the configuration, some modes with a high number can have significant contributions. For $(X_T = -4, Y_T = -12)$, 46 couples are required to obtain 95% of the total energy (the 47th couple involves 5%). Thus, each term of the solution will contribute in a different way for a given configuration as wide modification of the geometry of the plate could occur. To illustrate these discrepancies, a local error rate on some maximum values for u_3, σ_{22} and σ_{33} is showed in Fig. 7. It can be inferred from this figure that the accuracy of the results decreases at the bounds of the study domain for X_T, Y_T. Nevertheless, the error rate remains less than 2% for σ_{22} (corresponds to the direction of the traction). For the transverse normal stress, this error is about 15% as it is the most difficult quantity to improve, but it is localized near the bounds of the domain $[-4,4] \times [-12,12]$.

To illustrate the previous results, the 24 first normalized functions $v_1^i(x,y), v_2^i(x,y), v_3^i(x,y)$, the 32 first normalized $f_1^i(z), f_2^i(z), f_3^i(z)$ functions are shown in Figs. 8–13. For the functions $v_2^i(x,y)$ in the direction of the traction, the first 5 modes are global. It corresponds to the main contribution to the total strain energy. The corresponding correction in the transverse direction x is localized in an area near the hole over the whole width of the plate. Due to the type of solicitation, the associated transverse functions (cf. Figs. 11–13) are classically constant through the thickness for f_1^i, f_2^i and linear for f_3^i (Poisson effect). We also notice local modes. For instance, corrections all around of the circumference of the hole or in the vicinity of this one are obtained with mode 9 and 20 for both v_1 and v_2. The distribution of the associated $f_j^i(z)$ functions become more complex. Thus, the expression of the solution requires high-order z-expansion terms due to the presence of the hole.

The functions $g_X^i(X_T)$ and $g_Y^i(Y_T)$ associated to the location of the hole are also given in Fig. 14. They are not similar as the influence of the hole position is not the same in the two directions. We also notice a higher gradient of this function near the bound of the interval, especially for $g_X^i(X_T)$.

To assess the capability of the method, the distribution of σ_{22} from the hole to the free edge at the middle of the layer is shown in Fig. 15(a). It is compared with the results from LD4 model for three different locations of the hole. The results are in very good agreement with the reference solution. The high stress gradient near the hole is well captured regardless the configuration. Finally, the approach allows us to compute with accuracy for a low computational cost the distribution of the maximal value of σ_{22} with respect to the hole location as an explicit solution is obtained in this work. It is represented in Fig. 15(b). It can be noticed that

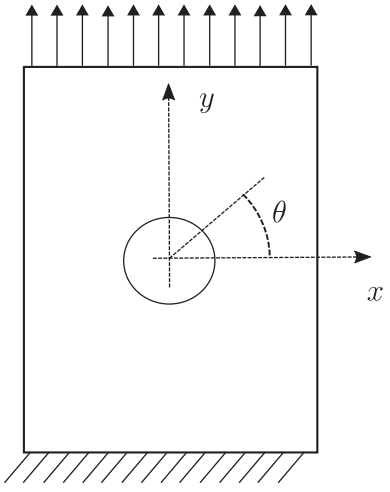

Fig. 4. Plate under uniaxial tension.

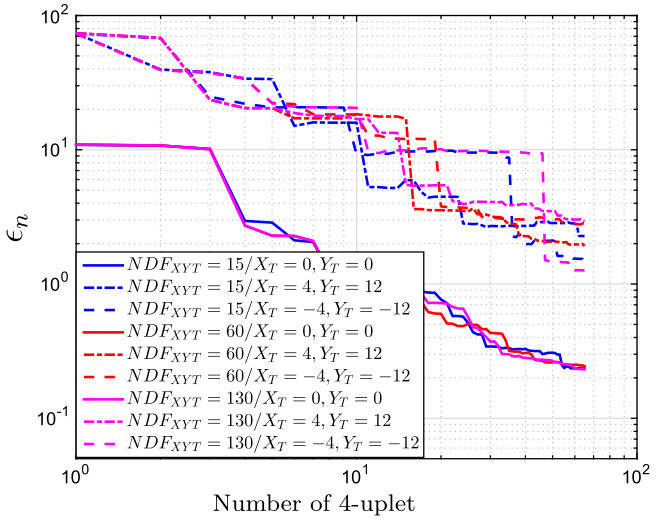

Fig. 5. Energy error for different number of elements associated to $g_X(X_T)$ and $Y(Y_T) - X_T \in [-4,4]$ and $Y_T \in [-12,12] - (X_T = -4, Y_T = -12), (X_T = 0, Y_T = 0), (X_T = 4, Y_T = 12)$.

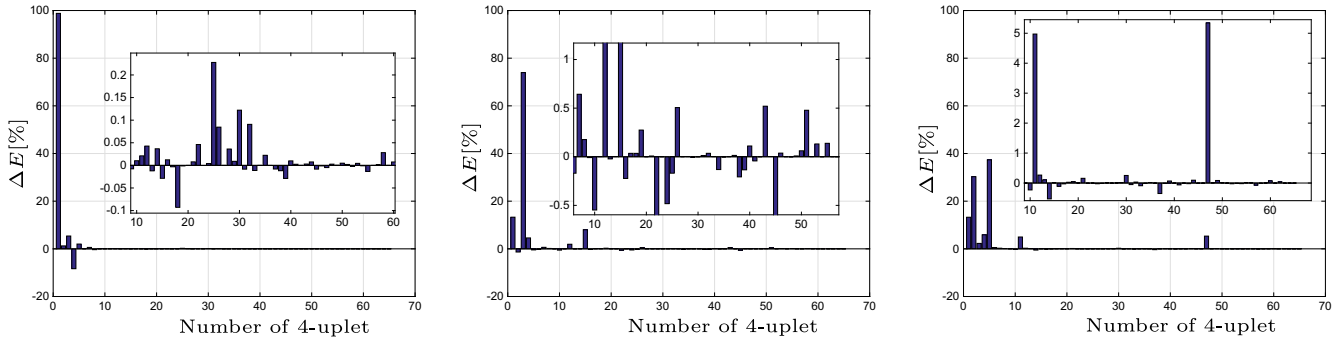

(a) $(X_T = 0, Y_T = 0)$ (b) $(X_T = 4, Y_T = 12)$ (c) $(X_T = -4, Y_T = -12)$

Fig. 6. Contribution of each couple to the total strain energy – $X_T \in [-4, 4]$ and $Y_T \in [-12, 12]$ – 65 couples.

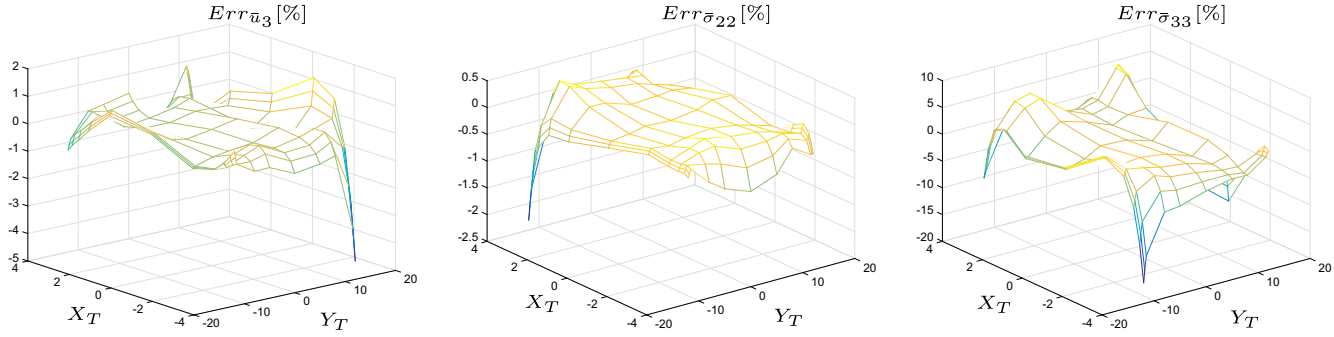

Fig. 7. Local error on the maximum value with respect to X_T and Y_T at the edge of the hole – $X_T \in [-4, 4]$ and $Y_T \in [-12, 12]$.

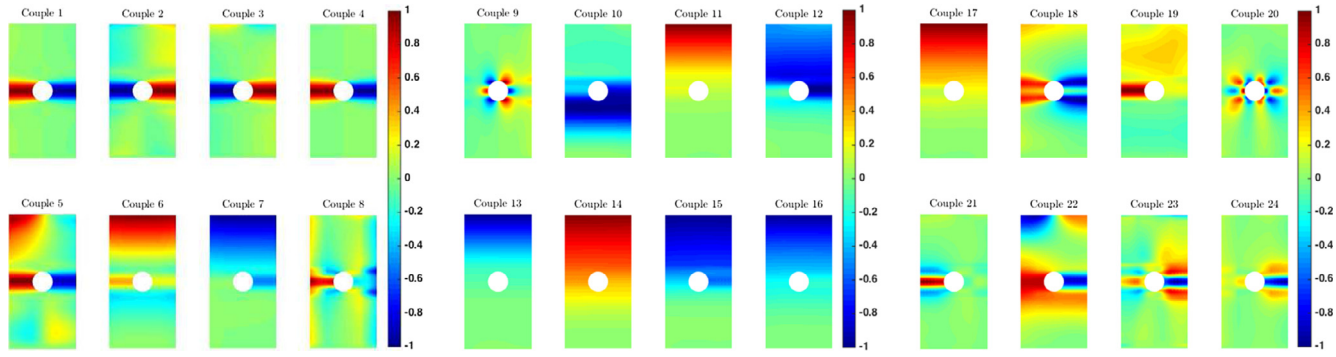

Fig. 8. Distribution of $v_1^i(x, y)$.

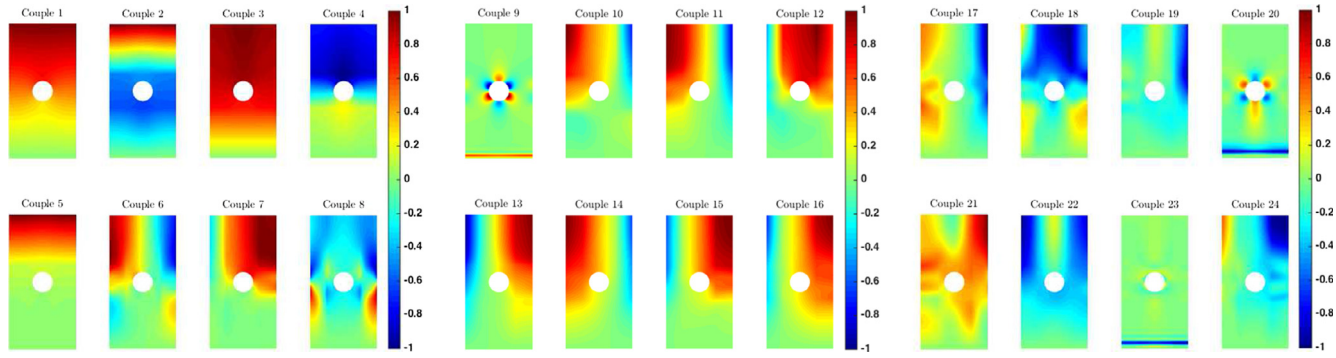

Fig. 9. Distribution of $v_2^i(x, y)$.

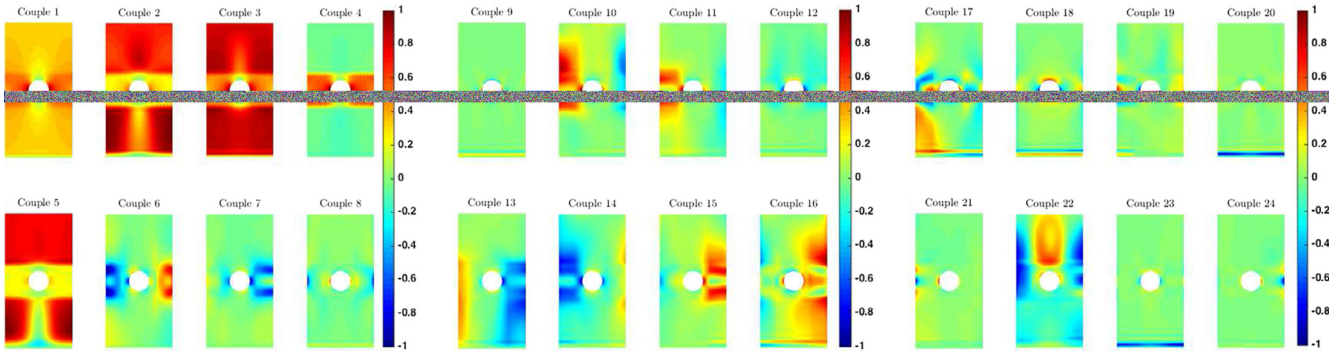

Fig. 10. Distribution of $v_3^i(x,y)$.

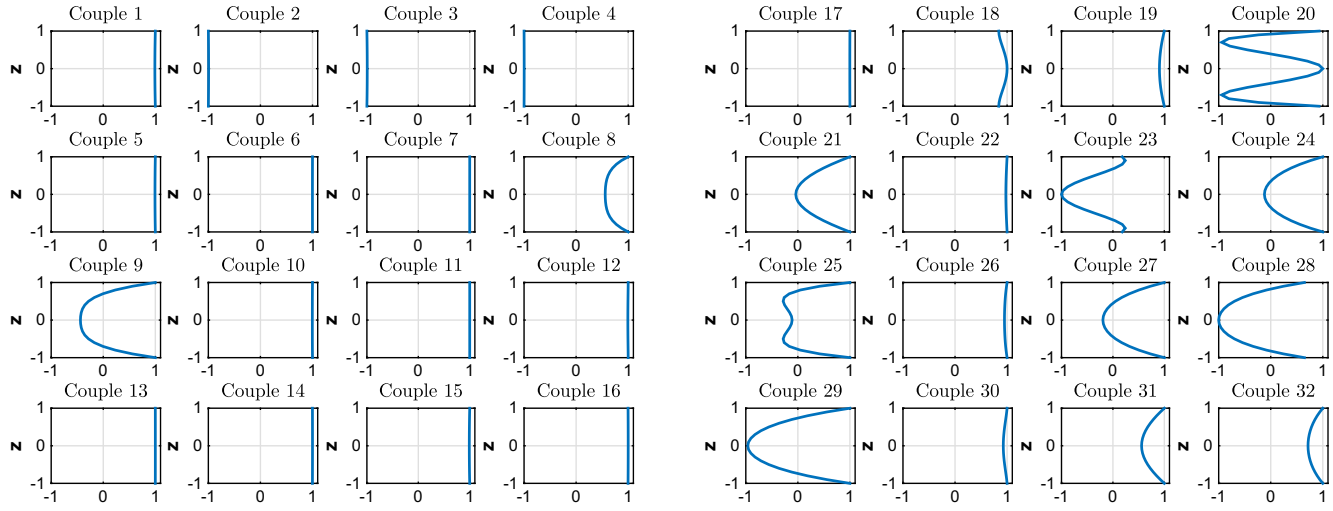

Fig. 11. Distribution of $f_1^i(x,y)$.

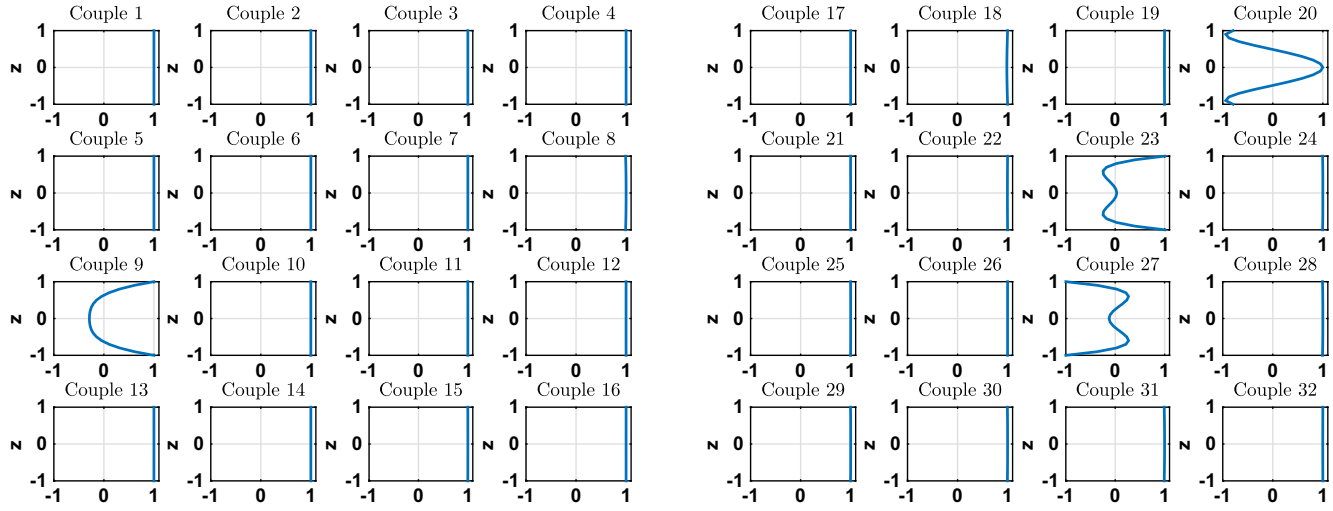

Fig. 12. Distribution of $f_2^i(x,y)$.

the stress concentration is more sensitive to the hole location in the width direction of the plate, as expected. In a classical approach, numerous computations are required to build this type of curve, as one point corresponds to one F.E. analysis.

4.3. Four-layer plate

In this section, a four-layer $[0°/90°/90°/0°]$ plate is considered with $\mathcal{I}_T = [-4.5, 4.5] \times [-13, 13]$. The choice of this new domain

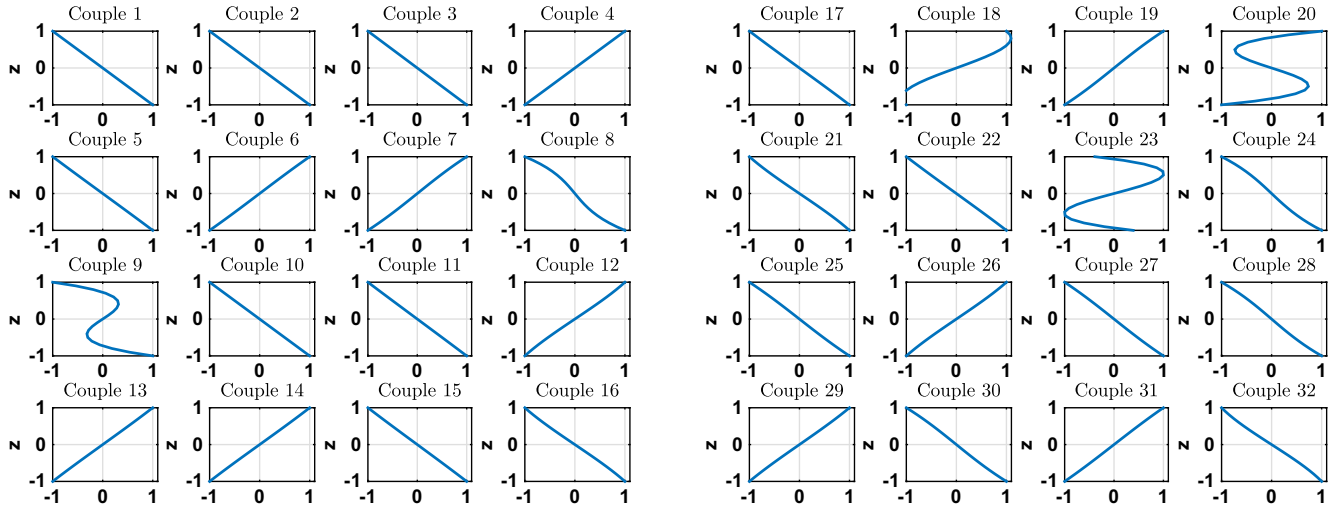

Fig. 13. Distribution of $f_3^i(x, y)$.

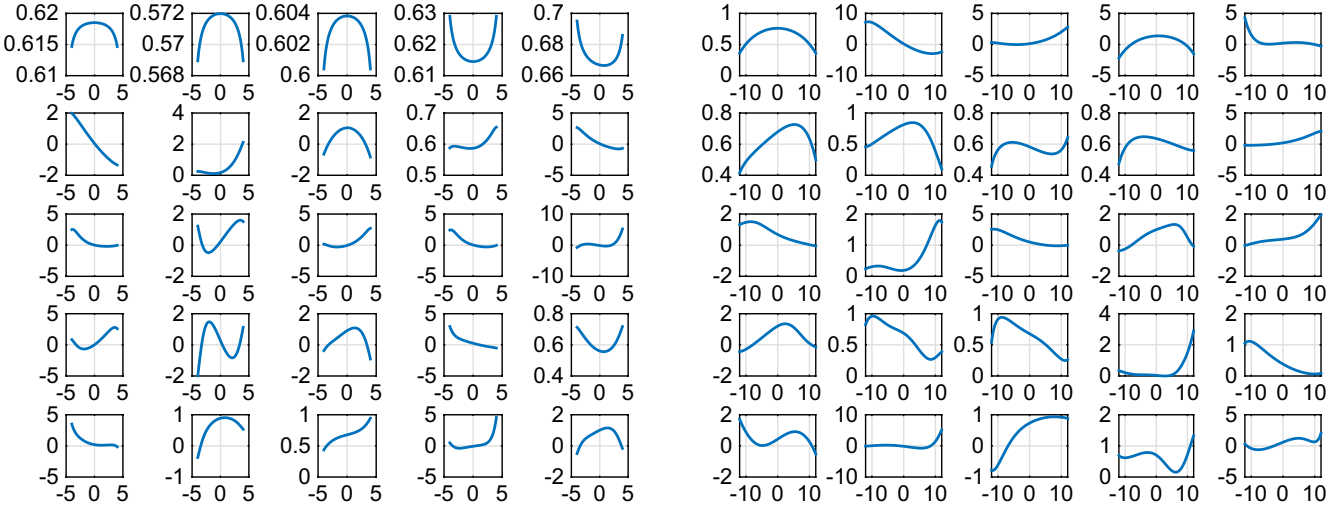

Fig. 14. Distribution of $g_X^i(X_T)$ (left) and $g_Y^i(Y_T)$ (right).

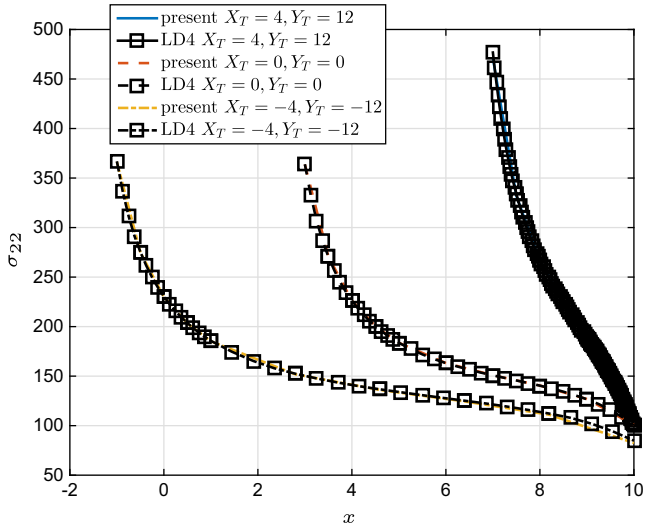

(a) distribution of $\bar{\sigma}_{22}$ at the middle of the layer (from hole to free edge)

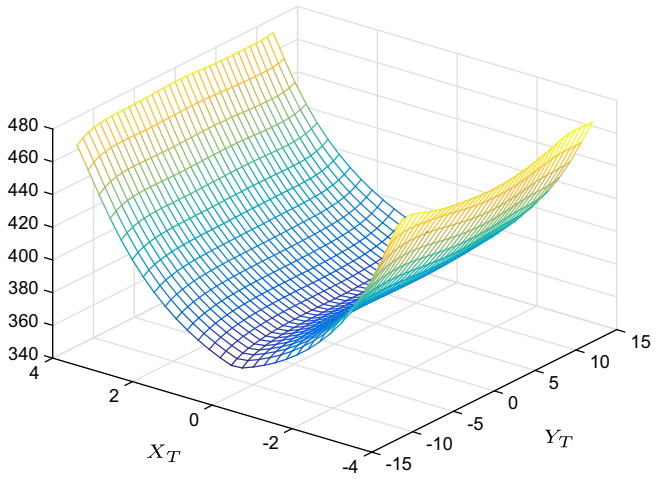

(b) $\sigma_{22\,max}$ with respect to X_T and Y_T

Fig. 15. 1 layer $[0^\circ] - X_T \in [-4, 4]$ and $Y_T \in [-12, 12]$.

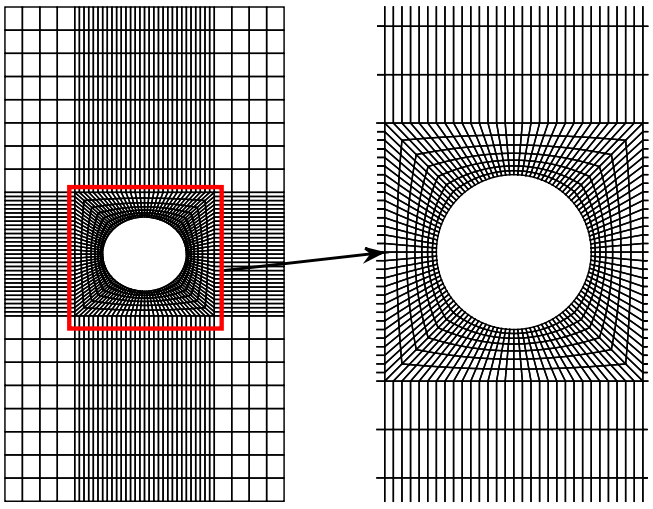

Fig. 16. Reference mesh – 4 layers.

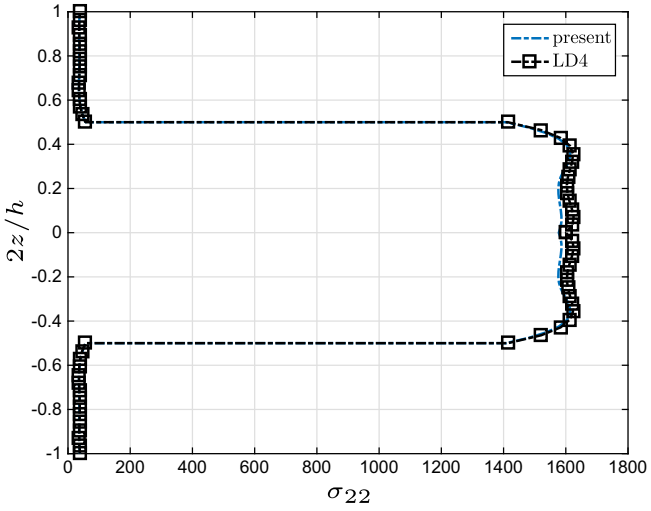

Fig. 18. Distribution of σ_{22} (left) and $\bar{\sigma}_{33}$ (right) along the thickness – 4 layers – $X_T = -4, Y_T = -12$.

comes from the previous study on a one-layer structure. The suitable mesh is shown in Fig. 16. The convergence study is not given for brevity reason. 75 4-uplets are used to recover the solution. The method is now assessed on the local results near the hole. For this purpose, the distributions of the displacements, the in-plane stress σ_{22}, the transverse stresses through the thickness for $X_T = -4$ and $Y_T = -12$ are shown in Figs. 17–19, respectively. This hole position is chosen as it is one of the most difficult configuration. The results of the present approach are in very good agreement with the LD4 model. The error rate on u_1 seems high but the value scale is about 10^{-8}. A zig-zag effect occurs for the transverse displacement and it would be impossible to capture this distribution with both classical but also higher-order ESL models. Transverse stresses fulfill the continuity requirement at the layer interface (see Fig. 19). For the transverse normal stress, the highest variation occurs near the interface layer $0°/90°$ (see Fig. 19 left).

For further assessment, the distributions of $\sigma_{\theta\theta}, \sigma_{zz}$ and $\sigma_{\theta z}$ along the circumference of the hole (one quarter) at the $0°/90°$ interface are given in Fig. 20. The accuracy of the present method is very good, and the different areas subjected to interlaminar compression or tension are well-identified, in particular for the transverse normal stress. This aspect could be of paramount importance in the prediction of the failure of the structure. Finally, the capability of the method to capture the steep stress gradient near the curved edge is illustrated in Fig. 21. The distribution of the transverse stresses σ_{33} and σ_{13} at the $0°/90°$ interface layer along the x axis shows the local effect that is well-represented when compared to the quasi-3D LD4 model. We also notice that the stress concentration factor is accurately predicted (cf. Fig. 21 left).

4.4. Localized stress near the hole for the 4-layer plate

In this last example, the thickness of the plate is decreased ($h = 0.5$) to localize the steep stress gradient near the hole. 115 couples are needed to recover the solution with accuracy. Distributions of stresses along the x axis at the bi-material interface for two configurations are given in Fig. 22. The levels of the transverse stresses and the stress concentration factor are well-estimated despite the high localization of the phenomenon near the hole and also the wide range of stresses. The efficiency of the method is proved for this discriminating test case.

Thus, the present approach allows us to provide 3D results confined in a small region, without the use of numerous 3D FE analysis. Indeed, the obtained solution with geometrical parameters allows us to have in a straightforward manner the displacements or stresses for any hole locations. Moreover, the solutions requires the resolution of only one 2D and three 1D problems, that is less expensive than 3D or LW analysis. For instance, the LD4 model requires 272,952 dofs while the present method involves 16,056 dofs for the 2D problem with 4 layers.

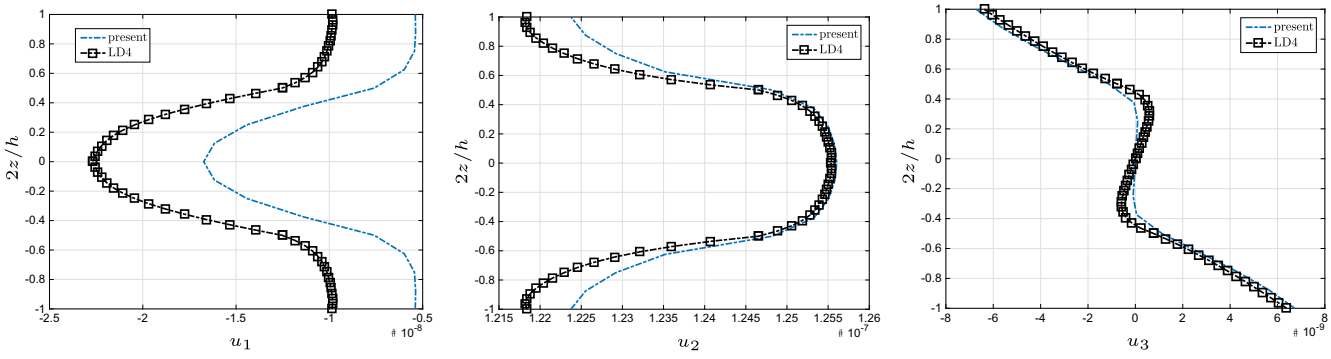

Fig. 17. Distribution of u_1 (left), u_2 (middle) and u_3 (right) along the thickness – 4 layers – $X_T = -4, Y_T = -12$.

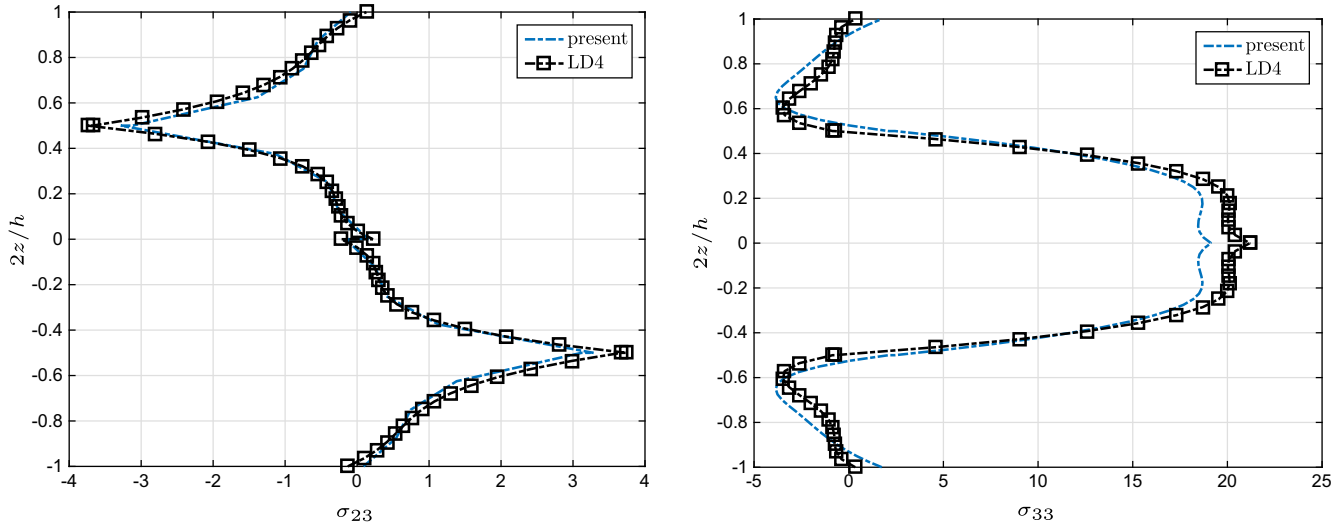

Fig. 19. Distribution of σ_{23} (left) and σ_{33} (right) along the thickness – 4 layers – $X_T = -4, Y_T = -12$.

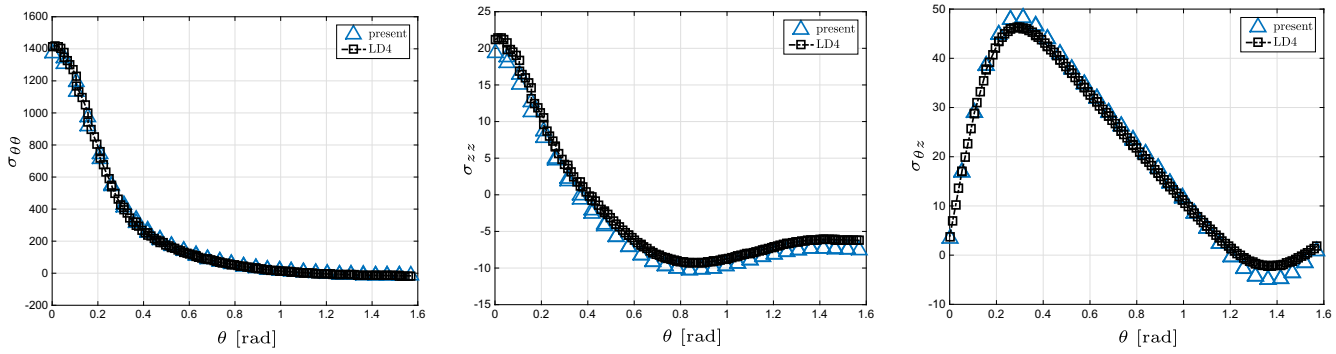

Fig. 20. Distribution of $\sigma_{\theta\theta}, \sigma_{zz}$ and $\sigma_{\theta z}$ around the hole at the $0^\circ/90^\circ$ interface – 4 layers – $X_T = -4, Y_T = -12$.

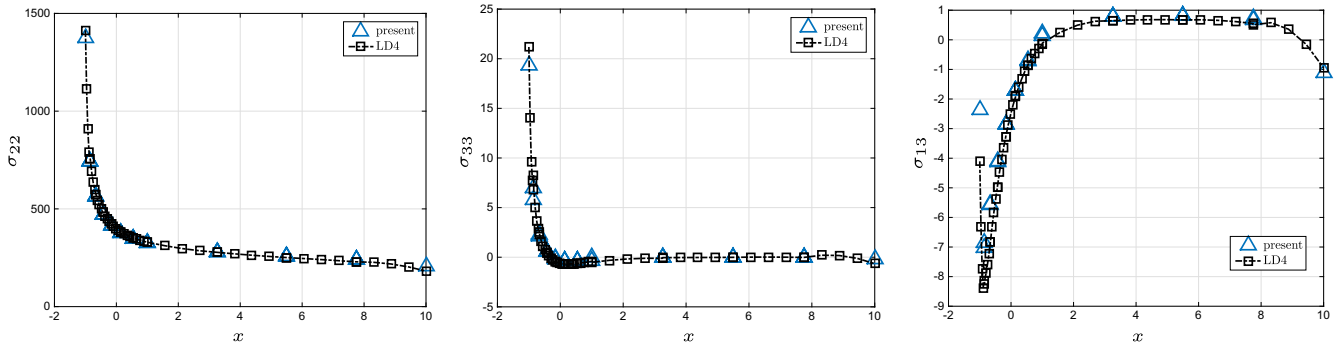

Fig. 21. Distribution of σ_{22} (left), σ_{33} (middle), and σ_{13} (right) from the free edge to the hole at the $0^\circ/90^\circ$ interface layer – 4 layers – $X_T \in [-4.5, 4.5]$ and $Y_T \in [-13, 13]$ – $X_T = -4, Y_T = -12$.

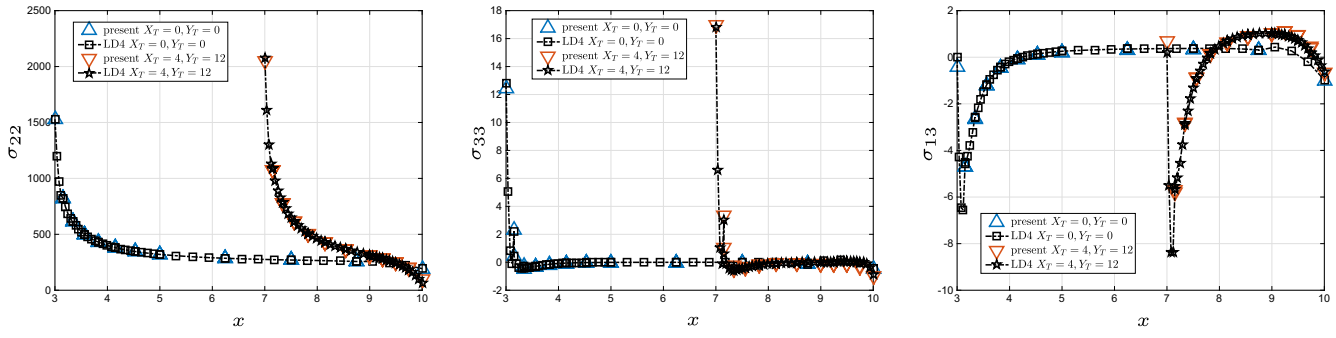

Fig. 22. σ_{22} (left), σ_{33} (middle), and σ_{13} (right) from the free edge to the hole at the $0^\circ/90^\circ$ interface layer – 4 layers – $X_T \in [-4.5, 4.5]$ and $Y_T \in [-13, 13]$ - $h = 0.5$.

5. Conclusion

In this work, a variable separation approach is proposed for the modeling of composite plate with arbitrary hole locations. The resolution of the geometrical parameterized problem is based on a mapping transformation of the sub-domains of the plate. A 8-node FE for the in-plane approximation is used for all unknowns. A fourth-order LW description of the thickness approximation is chosen. The approach has been studied and assessed on various laminates and geometries.

By comparing with higher-order LW models with a fixed location of the hole, it can be inferred from the results that the present approach has the capability to capture the steepest stress gradient near the curved free-edge. Indeed, the accuracy of the transverse stresses through the thickness at the hole is very good. Thus, quasi-3D results are provided. Moreover, the approach allows us to determine the influence of the hole position on the stresses or displacements as an explicit solution is built. Classically, it requires numerous expensive computations of LW or 3D models. Thus, the computational gain could be important. And, this one increases when the number of layers increases. The storage capacity involved in the present study is also reduced owing to the variables separation allowing to decrease the dimension of the problem. Therefore, this method seems to have very attractive features in the modeling of such a challenging test case for laminates.

Appendix A. Expression of T^p_{Xij}, T^p_{Yij}

$$T^p_{X11}=\tfrac{1}{j^p_{11}},\ T^p_{X12}=1,\ T^p_{X13}=\tfrac{1}{j^p_{11}},\ T^p_{Y11}=\tfrac{1}{j^p_{22}},\ T^p_{Y12}=\tfrac{1}{j^p_{22}},\ T^p_{Y13}=1$$

$$T^p_{X22}=j^p_{11},\ T^p_{X23}=1,\ T^p_{X33}=\tfrac{1}{j^p_{11}},\ T^p_{Y22}=\tfrac{1}{j^p_{22}},\ T^p_{Y23}=1,\ tY^p_{33}=j^p_{22} \tag{A.1}$$

Appendix B. Finite element problem to be solved on $_0$

This section is devoted to the calculation of $\boldsymbol{\sigma}^p_{zXY}(\tilde{f},\tilde{g}_X,\tilde{g}_Y,\mathbf{u}^m)$ in Eq. (26) under the product of one 2D and three 1D integrals. This term comes from the m known 4-uplets previously built in the greedy algorithm. Thus, we can define:

$$\begin{aligned}\boldsymbol{\sigma}^p_{zXY}(\tilde{f},\tilde{g}_X,\tilde{g}_Y,\mathbf{u}^m)&=\sum_{k=1}^{m}\boldsymbol{\sigma}^p_{zXY}(\tilde{f},\tilde{g}_X,\tilde{g}_Y,\mathbf{u}^k)\\&=\sum_{k=1}^{m}\int_{X_T}\int_{Y_T}\int_{\Omega_z}\left[\tilde{g}_X\tilde{g}_Y\,\mathcal{T}_\varepsilon^T\boldsymbol{\Sigma}_{\mathbf{z}}(\tilde{f})^T\mathbf{C}\boldsymbol{\varepsilon}(\mathbf{u}^k)\right]dzdX_TdY_T\end{aligned} \tag{B.1}$$

To separate the functions depending of the 5 unknowns $(x,y),z,X_T,Y_T$, we introduce:

$$\begin{aligned}&\mathbf{k}^{pk}_{zXY}\left(\tilde{f},f^k,\tilde{g}_X,g^k_X,\tilde{g}_Y,g^k_Y\right)\\&\quad=\sum_{\substack{1\leqslant i\leqslant 3\\1\leqslant j\leqslant 3\\ i\leqslant j}}\mathbf{k}_z(\tilde{f},f^k)\circ\mathbf{U}_{ij}\int_{X_T}\tilde{g}_Xg^k_XT^p_{Xij}dX_T\int_{Y_T}\tilde{g}_Yg^k_YT^p_{Yij}dY_T\end{aligned} \tag{B.2}$$

with

$$\mathbf{k}_z(\tilde{f},f^k)=\int_{\Omega_z}\boldsymbol{\Sigma}_{\mathbf{z}}(\tilde{f})^T\mathbf{C}\boldsymbol{\Sigma}_{\mathbf{z}}(f^k)dz \tag{B.3}$$

The matrix $\mathbf{U}_{ij}$ is defined in Eq. (27), T^p_{Xij} and T^p_{Yij} are given in Appendix A. The superscripts p and k are the number of the sub-domain and the number of the 4-uplets, respectively.

Finally, $\boldsymbol{\sigma}^p_{zXY}(\tilde{f},\tilde{g}_X,\tilde{g}_Y,\mathbf{u}^k)$ can be expressed as:

$$\boldsymbol{\sigma}^p_{zXY}(\tilde{f},\tilde{g}_X,\tilde{g}_Y,\mathbf{u}^k)=\mathbf{k}^{pk}_{zXY}\left(\tilde{f},f^k,\tilde{g}_X,g^k_X,\tilde{g}_Y,g^k_Y\right)\boldsymbol{\mathcal{E}}^k_v \tag{B.4}$$

Appendix C. Finite element problem to be solved on $\mathcal{I}_T$ for $g_Y(Y_T)$

The computation of the unknown function $\tilde{g}^{(k)}_Y$, denoted g_X, is described below, the other ones $\tilde{\mathbf{v}}^{(k-1)},\tilde{\mathbf{f}}^{(k-1)},\tilde{g}^{(k)}_X$ being known. They are denoted $\tilde{\mathbf{v}},\tilde{\mathbf{f}}$ and $\tilde{g}_X$, respectively.

The problem Eq. (17) can be solved in a straightforward manner following:

$$K_{xyzX}(\tilde{v},\tilde{f},\tilde{g}_X)\,g_Y=\mathcal{R}_{g_Yt}(\tilde{v},\tilde{f},\tilde{g}_X)-\mathcal{R}_{g_Y}(\tilde{v},\tilde{f},\tilde{g}_X,\mathbf{u}^m) \tag{C.1}$$

where we have

- the stiffness matrix

$$K_{xyzX}(\tilde{v},\tilde{f},\tilde{g}_X)=\sum_{p=1}^{NbArea}\sum_{\substack{1\leqslant i\leqslant 3\\1\leqslant j\leqslant 3\\ i\leqslant j}}E^p_{z\Omega\,ij}(\tilde{f},\tilde{v})\left[\int_{X_T}\tilde{g}_X^2T^p_{Xij}\,dX_T\right]T^p_{Yij}\Big|_{Y_T} \tag{C.2}$$

  $E^p_{z\Omega\,ij}(\tilde{f},\tilde{v})$ and $\mathbf{k}_z(\tilde{f}),\mathbf{U_{ij}}$ are given in Eqs. (38) and (27), respectively.
- the equilibrium residual

$$\mathcal{R}_{g_Yt}(\tilde{v},\tilde{f},\tilde{g}_X)=\left[\sum_{p=1}^{NbArea}\int_{\Gamma^p_N}\tilde{\mathbf{v}}^T\left(\int_{X_T}\tilde{g}_X\frac{1}{j^p_{11}}dX_T\right)dx^p\right]\mathbf{t}_z(\tilde{f}) \tag{C.3}$$

$\mathcal{R}_{g_Y}(\tilde{v},\tilde{f},\tilde{g}_X,\mathbf{u}^m)$ is built from the known function $\mathbf{u}^m$. It is computed in the same way as K_{xyzX}.

References

[1] Mittelstedt C, Becker W. Interlaminar stress concentrations in layered structures: Part I – A selective literature survey on the free-edge effect since 1967. J Comput Mater 2004;38:1037–62.
[2] Mittelstedt C, Becker W. Free-edge effects in composite laminates. Appl Mech Rev 2007;60:217–45.
[3] Rybicki E, Schmueser D. Effect of stacking sequence and lay-up angle on free edge stresses around a hole in a laminated plate under tension. J Comput Mater 1978;12:300–13.
[4] Crews J, Raju L. Three-dimensional analysis of $[0/90]_s$ and $[90/0]_s$ laminates with a central circular hole. J Compos Technol Res 1982;4(4):116–24.
[5] Carlsson L. Interlaminar stresses at a hole in a composite member subjected to in-plane loading. J Comput Mater 1983;17:238–49.
[6] Lucking W, Hoa S, Sankar T. The effect of geometry on interlaminar stresses of $[0/90]_s$ composite laminates with circular holes. J Comput Mater 1984;17:188–98.
[7] Hu F, Soutis C, Edge E. Interlaminar stresses in composite laminates with a circular hole. Compos Struct 1997;37:223–32.
[8] Raghuram P, Murty A. A high precision coupled bending-extension triangular finite element for laminated plates. Comput Struct 1999;72:763–77.
[9] Lin C-C, Kuo C-S. Buckling of laminated plates with holes. J Comput Mater 1989;23:536–53.
[10] Liu G, Tay T, Tan V. Failure progression and mesh sensitivity analyses by the plate element-failure method. J Comput Mater 2010;44:2363–79.
[11] Ramesh S, Wang C, Reddy J, Ang K. A higher-order plate element for accurate prediction of interlaminar stresses in laminated composite plates. Compos Struct 2009;91:337–57.
[12] Barboni R, Carbonaro R, Gaudenzi P. On the use of a multilayer higher-order theory for the stress analysis around a circular hole of laminates under tension. Compos Struct 1995;32:649–58.
[13] Ahn J, Kim Y-W, Woo K-S. Analysis of circular free edge effect in composite laminates by p-convergent global-local model. Int J Mech Sci 2013;66:149–55.
[14] Zhen W, Wanji C. Stress analysis of laminated composite plates with a circular hole according to a single-layer higher-order model. Compos Struct 2009;90:122–9.
[15] Pian THH, Li MS. Stress analysis of laminated composites by hybrid finite elements. In: Kuhn G, Mang H, editors. Discretization methods in structural mechanics: IUTAM/IACM symposium Vienna, Austria, 1989. Springer-Verlag; 1990. p. 363–72.
[16] Ammar A, Mokdada B, Chinesta F, Keunings R. A new family of solvers for some classes of multidimensional partial differential equations encountered in kinetic theory modeling of complex fluids. J Non-Newton Fluid Mech 2006;139:153–76.
[17] Savoia M, Reddy J. A variational approach to three-dimensional elasticity solutions of laminated composite plates. J Appl Mech ASME 1992;59:166–75.

[18] Bognet B, Bordeu F, Chinesta F, Leygue A, Poitou A. Advanced simulation of models defined in plate geometries: 3D solutions with 2D computational complexity. Comput Methods Appl Mech Eng 2012;201–204:1–12. http://dx.doi.org/10.1016/j.cma.2011.08.025.
[19] Vidal P, Gallimard L, Polit O. Proper generalized decomposition and layer-wise approach for the modeling of composite plate structures. Int J Solids Struct 2013;50(14–15):2239–50. http://dx.doi.org/10.1016/j.ijsolstr.2013.03.034.
[20] Polit O, Gallimard L, Vidal P, D'Ottavio M, Giunta G, Belouattar S. An analysis of composite beams by means of hierarchical finite elements and a variables separation method. Comput Struct 2015;158:15–29. http://dx.doi.org/10.1016/j.compstruc.2015.05.033.
[21] Giunta G, Belouattar S, Polit O, Gallimard L, Vidal P, D'Ottavio M. Hierarchical beam finite elements based upon a variables separation method. Int J Appl Mech 2016;8(2):1650026–35. http://dx.doi.org/10.1142/S1758825116500265.
[22] Vidal P, Gallimard L, Polit O. Assessment of variable separation for finite element modeling of free edge effect for composite plates. Compos Struct 2015;123(–):19–29. http://dx.doi.org/10.1016/j.compstruct.2014.11.068.
[23] Lassila T, Rozza G. Parametric free-form shape design with PDE models and reduced basis method. Comput Methods Appl Mech Eng 2010;199:1583–92.
[24] Ammar A, Huerta A, Chinesta F, Cueto E, leygue A. Parametric solutions involving geometry: a step towards efficient shape optimization. Comput Methods Appl Mech Eng 2014;268:178–93.
[25] Courard A, Néron D, Ladevèze P, Ballere L. Integration of PGD-virtual charts into an engineering design process. Comput Mech 2016;57:637–51.
[26] Sukumar N, Chopp D, Moes N, Belytschko T. Modeling holes and inclusions by level sets in the extended finite-element method. Comput Methods Appl Mech Eng 2001;190:6183–200.
[27] Nouy A, Chevreuil M, Safatly E. Fictitious domain method and separated representations for the solution of boundary value problems on uncertain parameterized domains. Comput Methods Appl Mech Eng 2011;200:3066–82. http://dx.doi.org/10.1016/j.cma.2011.07.002.
[28] Icten B, Sayman O. Failure analysis of pin-loaded aluminum-glass-epoxy sandwich composite plates. Compos Sci Technol 2003;63(5):727–37. http://dx.doi.org/10.1016/S0266-3538(02)00260-9.
[29] Carrera E. Theories and finite elements for multilayered, anisotropic, composite plates and shells. Arch Comput Meth Eng 2002;9:87–140.
[30] Vidal P, Gallimard L, Polit O. Shell finite element based on the proper generalized decomposition for the modeling of cylindrical composite structures. Comput Struct 2014;132:1–11. http://dx.doi.org/10.1016/j.compstruc.2013.10.015.
[31] Carrera E, Demasi L. Classical and advanced multilayered plate elements based upon PVD and RMVT. Part 1: Derivation of finite element matrices. Int J Num Meth Eng 2002;55:191–231.
[32] Carrera E, Demasi L. Classical and advanced multilayered plate elements based upon PVD and RMVT. Part 2: Numerical implementations. Int J Num Meth Eng 2002;55:253–91.